

# ISOGEOMETRIC MULTILEVEL QUADRATURE FOR FORWARD AND INVERSE RANDOM ACOUSTIC SCATTERING

JÜRGEN DÖLZ, HELMUT HARBRECHT, CARLOS JEREZ-HANCKES,  
AND MICHAEL MULTERER

ABSTRACT. We study the numerical solution of forward and inverse acoustic scattering problems by randomly shaped obstacles in three-dimensional space using a fast isogeometric boundary element method. Within the isogeometric framework, realizations of the random scatterer can efficiently be computed by simply updating the NURBS mappings which represent the scatterer. This way, we end up with a random deformation field. In particular, we show that the knowledge of the deformation field's expectation and covariance at the surface of the scatterer are already sufficient to **model** the surface Karhunen-Loève expansion. Leveraging on the isogeometric framework, we utilize multilevel quadrature methods for the efficient approximation of quantities of interest, such as the scattered wave's expectation and variance. Computing the wave's Cauchy data at an artificial, fixed interface enclosing the random obstacle, we can also directly infer quantities of interest in free space. Adopting the Bayesian paradigm, we finally compute the expected shape and the variance of the scatterer from noisy measurements of the scattered wave at the artificial interface. Numerical results for the forward and inverse problem are given to demonstrate the feasibility of the proposed approach.

## 1. INTRODUCTION

The reliable computer simulation of phenomena where acoustic waves are scattered by obstacles is of great importance in many applications. These include for example the modelling of sonar and other methods of acoustic location, as well as outdoor noise propagation and control, especially stemming from automobiles, railways or aircrafts. Since an analytical solution of scattering problems is in general impossible, numerical approaches are called for.

Most acoustic scattering problems may be formulated in the frequency domain by employing the Helmholtz equation: assume an acoustic wave encounters an impenetrable, bounded obstacle  $D \subset \mathbb{R}^3$ , having a Lipschitz smooth boundary  $S := \partial D$ , and, as a consequence, gets scattered. Then, describing the incident plane wave  $u_{\text{inc}}(\mathbf{x}) = e^{i\kappa\langle \mathbf{d}, \mathbf{x} \rangle}$  with known wavenumber  $\kappa$  and direction  $\mathbf{d}$ , where  $\|\mathbf{d}\|_2 = 1$ , the

total wave

$$u = u_{\text{inc}} + u_{\text{s}}$$

is obtained by solving the exterior boundary value problem

$$(1.1) \quad \begin{aligned} \Delta u + \kappa^2 u &= 0 && \text{in } \mathbb{R}^3 \setminus \overline{D}, \\ u &= 0 && \text{on } S, \\ \sqrt{r} \left( \frac{\partial u_{\text{s}}}{\partial r} - i\kappa u_{\text{s}} \right) &\rightarrow 0 && \text{as } r = \|\mathbf{x}\|_2 \rightarrow \infty. \end{aligned}$$

The homogeneous Dirichlet condition at  $S$  corresponds to a *sound-soft* obstacle, whereas a homogeneous Neumann condition would correspond to a *sound-hard* obstacle. The function  $u_{\text{s}} = u - u_{\text{inc}}$  is called the *scattered wave*. Although we restrict ourselves to the sound-soft case, the presented concepts are also suitable to treat sound-hard obstacles as well as for penetrable obstacles, i.e. objects described by a different diffractive index to the free space.

In this article, we consider the situation of a randomly shaped obstacle  $D = D(\mathbf{y})$ , where  $\mathbf{y} \in \Gamma \subset \mathbb{R}^{\mathbb{N}}$  is some random parameter. This shape uncertainty might for example issue from measurement or modelling errors. As a consequence, the total wave itself becomes a random field  $u(\mathbf{y})$ . Our goal is to compute the first and second order statistics of the scattered wave, these are the expectation  $\mathbb{E}[u_{\text{s}}]$  and the variance  $\mathbb{V}[u_{\text{s}}]$ . We especially demonstrate how to compute the scattered wave's second moment in a deterministic fashion from its Cauchy data's second moment on an artificial, fixed interface  $T$ , which almost surely encloses the domain  $D(\mathbf{y})$ . In combination with low-rank techniques, this drastically reduces the high dimensionality of the random scattering problem, compare [25]. In order to speed up the computations of the Cauchy data's statistics even further, we employ the multilevel quadrature method, see e.g. [2, 19, 29, 32].

Our approach lies in the *domain mapping* category as it transfers the shape uncertainty onto a fixed reference domain, and allows to deal with large deformations (see [1, 37]). In contrast, *perturbation techniques* resort to shape derivatives to linearize fields for small deviations with respect to both wavelength and scatterers' shape from a nominal, reference geometry. By Hadamard's theorem, the resulting linearized equations for the first order shape sensitivities are homogeneous equations posed on the nominal geometry, with inhomogeneous boundary data only. Using first-order shape Taylor expansions, one can derive deterministic tensor first-kind boundary integral equations for the statistical moments of the scattering problems considered. These are then approximated by sparse tensor Galerkin discretizations via the combination technique (*cf.* [17] and references therein). Though successfully

applied to three-dimensional Helmholtz Dirichlet, Neumann, impedance and transmission problems [17], and even for diffraction gratings [43], therein random perturbations are required to be sufficiently small. High-order approaches [11, 27] lead to at least third order accurate approximations with respect to the perturbation amplitude of the domain variations. Finally, in [7] a hybrid between domain-mapping and perturbation methods was presented.

For the numerical realization of random obstacles, we employ the methodology from *isogeometric analysis* (IGA). IGA has been introduced in [35] in order to incorporate simulation techniques into the design workflow of industrial development and thus allows to deal with domain deformations in a straightforward manner. By representing the geometry and domain deformations by *non-uniform rational B-splines* (NURBS), realizations of the random scatterer can efficiently be computed by simply updating the NURBS mappings which represent the scatterer. In addition, the naturally emerging sequence of nested approximation spaces can directly be employed in multilevel quadrature methods. With regard to the isogeometric boundary element approach for the scattered wave computations, compare [14, 18, 44, 45], we show that all computations can directly be performed at the boundary of the deformed scatterer. This particularly applies to the random deformation field which only needs to be computed with respect to a reference surface. This way, we can model large deformations without having to deal with very fine volume meshes, which would otherwise be necessary to properly resolve the deformation field within the scatterer. Moreover, the meshing of the unbounded free space is avoided. Therefore, the isogeometric boundary element method is the method of choice for the problem at hand. For the numerical computations, we rely on the fast isogeometric boundary element method developed in [13–16, 26], which is available as C++ library `bemvel` [12, 13]. In order to speed up computations, `bemvel` utilizes  $\mathcal{H}^2$ -matrices with the interpolation based fast multipole method [20–22].

To our knowledge, the present work constitutes the first fast IGA implementation for time-harmonic acoustic wave scattering for shape uncertainty quantification. Having this fast forward solver at our disposal, we also consider acoustic shape inversion by Bayesian inference: Given noisy measurements of the scattered wave at certain locations in free space, we determine statistics of the uncertain scatterer’s shape. To this end, we employ the multilevel ratio estimator, see [10] and the references therein, and compute the expected shape and its variance.

The rest of article is organized as follows: Section 2 is concerned with the modelling of random domains and their parametrization by means of a Karhunen-Loève expansion. In Section 3, we perform the efficient discretization of the random deformation field by means of isogeometric analysis. In Section 4, we introduce the boundary integral formulation of the problem under consideration and discuss the use of the artificial interface for the representation of the scattered wave and its statistics. Section 5 briefly recalls the multilevel quadrature method, whereas Section 6 deals with its application to Bayesian inference. Finally, Section 7 is devoted to numerical examples showcasing the ideas discussed.

## 2. RANDOM DOMAIN MODEL

**2.1. Modelling of random domains.** In what follows, let  $D_{\text{ref}} \subset \mathbb{R}^3$  denote a Lipschitz domain with piecewise smooth surface  $S_{\text{ref}} := \partial D_{\text{ref}}$  and let  $(\Omega, \mathcal{F}, \mathbb{P})$  be a complete probability space. We assume that the uncertainty in the obstacle is encoded by a random deformation field, cf. [30]. We hence assume the existence of a uniform  $C^1$ -diffeomorphism  $\chi_D: \overline{D_{\text{ref}}} \times \Omega \rightarrow \mathbb{R}^3$ , i.e.

$$(2.1) \quad \|\chi_D(\omega)\|_{C^1(\overline{D_{\text{ref}}}; \mathbb{R}^3)}, \|\chi_D^{-1}(\omega)\|_{C^1(\overline{D(\omega)}; \mathbb{R}^3)} \leq C_{\text{uni}} \quad \text{for } \mathbb{P}\text{-a.e. } \omega \in \Omega,$$

such that

$$D(\omega) = \chi_D(D_{\text{ref}}, \omega).$$

Particularly, since  $\chi_D \in L^\infty(\Omega; [C^1(\overline{D_{\text{ref}}})]^3) \subset L^2(\Omega; [C^1(\overline{D_{\text{ref}}})]^3)$ , the deformation field  $\chi_D$  can be **expressed** by a Karhunen-Loève expansion [38] which has the form

$$(2.2) \quad \chi_D(\hat{\mathbf{x}}, \omega) = \mathbb{E}[\chi_D](\hat{\mathbf{x}}) + \sum_{k=1}^{\infty} \sqrt{\lambda_{D,k}} \chi_{D,k}(\hat{\mathbf{x}}) Y_{D,k}(\omega), \quad \hat{\mathbf{x}} \in D_{\text{ref}}.$$

Herein,

$$\mathbb{E}[\chi_D](\hat{\mathbf{x}}) := \int_{\Omega} \chi_D(\hat{\mathbf{x}}, \omega) \, d\mathbb{P}(\omega)$$

is the field's expectation, while  $(\lambda_{D,k}, \chi_{D,k})$  are the eigenpairs of the covariance operator  $\mathcal{C}_D: [L^2(D)]^3 \rightarrow [L^2(D)]^3$ ,

$$(2.3) \quad (\mathcal{C}_D \mathbf{U})(\hat{\mathbf{x}}) := \int_{D_{\text{ref}}} \text{Cov}[\chi_D](\hat{\mathbf{x}}, \hat{\mathbf{x}}') \mathbf{U}(\hat{\mathbf{x}}') \, d\hat{\mathbf{x}}',$$

where **the matrix valued covariance function is given by**

$$\text{Cov}[\chi_D](\hat{\mathbf{x}}, \hat{\mathbf{x}}') := \int_{\Omega} (\chi_D(\hat{\mathbf{x}}, \omega) - \mathbb{E}[\chi_D](\hat{\mathbf{x}})) (\chi_D(\hat{\mathbf{x}}', \omega) - \mathbb{E}[\chi_D](\hat{\mathbf{x}}'))^\top \, d\mathbb{P}(\omega).$$

It holds that

$$(2.4) \quad Y_{D,k}(\omega) := \frac{1}{\sqrt{\lambda_{D,k}}} \int_{D_{\text{ref}}} (\boldsymbol{\chi}_D(\widehat{\boldsymbol{x}}, \omega) - \mathbb{E}[\boldsymbol{\chi}_D](\widehat{\boldsymbol{x}}))^\top \boldsymbol{\chi}_{D,k}(\widehat{\boldsymbol{x}}) \, d\widehat{\boldsymbol{x}}.$$

The family  $\{Y_{D,k}\}_k$  of random variables is therefore uncorrelated and centred. We remark that in uncertainty quantification problems typically **only the spatial quantities**  $\mathbb{E}[\boldsymbol{\chi}_D]$  and  $\text{Cov}[\boldsymbol{\chi}_D]$  are known, such that the **distribution of the** random variables cannot be inferred via (2.4). Instead, their common distribution has to be appropriately **modelled**.

**2.2. Modelling of random surfaces.** The numerical computation of a Karhunen-Loève expansion as outlined in the previous subsection will generally requires a volume finite element mesh for  $D_{\text{ref}}$ . Moreover, the data  $\mathbb{E}[\boldsymbol{\chi}_D]$  and  $\text{Cov}[\boldsymbol{\chi}_D]$  need to be known for the entire reference domain  $D_{\text{ref}}$ . In contrast, for our boundary element-based approach, we only require realizations of the perturbed boundary. The following exposition shows that, for the computation of surface realizations, the knowledge of  $\mathbb{E}[\boldsymbol{\chi}_D]$  and  $\text{Cov}[\boldsymbol{\chi}_D]$  at the boundary  $S_{\text{ref}} = \partial D_{\text{ref}}$  is sufficient.

Given a function  $\boldsymbol{g}: D_{\text{ref}} \rightarrow \mathbb{R}^3$ , let

$$(\gamma_0^{\text{int}} \boldsymbol{g})(\widehat{\boldsymbol{x}}) := \lim_{\widehat{\boldsymbol{x}}' \ni D_{\text{ref}} \rightarrow \widehat{\boldsymbol{x}} \in S_{\text{ref}}} \boldsymbol{g}(\widehat{\boldsymbol{x}}')$$

denote the interior trace operator and let  $\boldsymbol{\chi}_S := \gamma_0^{\text{int}} \boldsymbol{\chi}_D$ . Since

$$\gamma_0^{\text{int}}: [C^1(\overline{D_{\text{ref}}})]^3 \subset [H^1(D_{\text{ref}})]^3 \rightarrow [H^{1/2}(S_{\text{ref}})]^3$$

is a continuous operator and the Bochner integral commutes with continuous operators, [33], it holds

$$(\gamma_0^{\text{int}} \mathbb{E}[\boldsymbol{\chi}_D])(\widehat{\boldsymbol{x}}) = \gamma_0^{\text{int}} \int_{\Omega} \boldsymbol{\chi}_D(\widehat{\boldsymbol{x}}, \omega) \, d\mathbb{P}(\omega) = \int_{\Omega} \boldsymbol{\chi}_S(\widehat{\boldsymbol{x}}, \omega) \, d\mathbb{P}(\omega) = \mathbb{E}[\boldsymbol{\chi}_S](\widehat{\boldsymbol{x}})$$

as well as

$$\begin{aligned} & (\gamma_0^{\text{int}} \otimes \gamma_0^{\text{int}}) \text{Cov}[\boldsymbol{\chi}_D](\widehat{\boldsymbol{x}}, \widehat{\boldsymbol{x}}') \\ &= \int_{\Omega} ((\gamma_0^{\text{int}} \boldsymbol{\chi}_D)(\widehat{\boldsymbol{x}}, \omega) - (\gamma_0^{\text{int}} \mathbb{E}[\boldsymbol{\chi}_D])(\widehat{\boldsymbol{x}})) \\ & \quad \cdot ((\gamma_0^{\text{int}} \boldsymbol{\chi}_D)(\widehat{\boldsymbol{x}}', \omega) - (\gamma_0^{\text{int}} \mathbb{E}[\boldsymbol{\chi}_D])(\widehat{\boldsymbol{x}}'))^\top \, d\mathbb{P}(\omega) \\ &= \int_{\Omega} (\boldsymbol{\chi}_S(\widehat{\boldsymbol{x}}, \omega) - \mathbb{E}[\boldsymbol{\chi}_S](\widehat{\boldsymbol{x}})) (\boldsymbol{\chi}_S(\widehat{\boldsymbol{x}}', \omega) - \mathbb{E}[\boldsymbol{\chi}_S](\widehat{\boldsymbol{x}}'))^\top \, d\mathbb{P}(\omega) \\ &= \text{Cov}[\boldsymbol{\chi}_S](\widehat{\boldsymbol{x}}, \widehat{\boldsymbol{x}}'). \end{aligned}$$

Therefore, the **the spatial structure of the** random deformation field at  $S$ , i.e.  $\boldsymbol{\chi}_S(\widehat{\boldsymbol{x}}, \omega)$ , **is fully encoded by the boundary quantities**

$$(\gamma_0^{\text{int}} \mathbb{E}[\boldsymbol{\chi}_D])(D) \quad \text{and} \quad (\gamma_0^{\text{int}} \otimes \gamma_0^{\text{int}}) \text{Cov}[\boldsymbol{\chi}_D](\widehat{\boldsymbol{x}}, \widehat{\boldsymbol{x}}').$$

For the numerical computation of the deformation field, it is therefore sufficient to only compute the eigenpairs  $(\lambda_{S,k}, \boldsymbol{\chi}_{S,k})$  of the surface covariance operator

$$\mathcal{C}_S: [L^2(S_{\text{ref}})]^3 \rightarrow [L^2(S_{\text{ref}})]^3$$

given by

$$(2.5) \quad (\mathcal{C}_{S_{\text{ref}}} \boldsymbol{U})(\widehat{\boldsymbol{x}}) := \int_{S_{\text{ref}}} (\gamma_0^{\text{int}} \otimes \gamma_0^{\text{int}}) \text{Cov}[\boldsymbol{\chi}_D](\widehat{\boldsymbol{x}}, \widehat{\boldsymbol{x}}') \boldsymbol{U}(\widehat{\boldsymbol{x}}') \, d\sigma_{\widehat{\boldsymbol{x}}'},$$

to obtain

$$(2.6) \quad \boldsymbol{\chi}_S(\widehat{\boldsymbol{x}}, \omega) = \gamma_0^{\text{int}} \mathbb{E}[\boldsymbol{\chi}_D](\widehat{\boldsymbol{x}}) + \sum_{k=1}^{\infty} \sqrt{\lambda_{S,k}} \boldsymbol{\chi}_{S,k}(\widehat{\boldsymbol{x}}) Y_{S,k}(\omega)$$

with

$$Y_{S,k}(\omega) := \frac{1}{\sqrt{\lambda_{S,k}}} \int_S (\boldsymbol{\chi}_S(\widehat{\boldsymbol{x}}, \omega) - \gamma_0^{\text{int}} \mathbb{E}[\boldsymbol{\chi}_D](\widehat{\boldsymbol{x}}))^\top \boldsymbol{\chi}_{S,k}(\widehat{\boldsymbol{x}}) \, d\sigma_{\widehat{\boldsymbol{x}}}.$$

**Similar to the volume case, the common distribution of the  $Y_{S,k}(\omega)$  needs to be appropriately estimated.**

We remark that the computation of the eigenpairs of (2.5) is significantly cheaper than the computation of the ones of (2.3) since the latter only relies on a surface mesh for  $S_{\text{ref}}$  rather than on a volume mesh for  $D_{\text{ref}}$ . Thus, the discrete system will be significantly smaller. However, the corresponding eigenfunctions will in general not be traces of the eigenfunctions of the Karhunen-Loève expansion (2.2) and, therefore, also the distribution of the random variables will change.

In the sequel, we assume that the family  $\{Y_{S,k}\}_k$  is independent and uniformly distributed with  $\{Y_{S,k}\}_k \sim \mathcal{U}(-1, 1)$  for all  $k$ . Then, we can identify each of the random variables by its image  $y_k \in [-1, 1]$  and up with the parametric deformation field

$$(2.7) \quad \boldsymbol{\chi}_S(\widehat{\boldsymbol{x}}, \boldsymbol{y}) = \gamma_0^{\text{int}} \mathbb{E}[\boldsymbol{\chi}_D](\widehat{\boldsymbol{x}}) + \sum_{k=1}^{\infty} \sqrt{\lambda_{S,k}} \boldsymbol{\chi}_{S,k}(\widehat{\boldsymbol{x}}) y_k, \quad \boldsymbol{y} \in \Gamma := [-1, 1]^{\mathbb{N}},$$

which gives rise to the random surface

$$(2.8) \quad S(\boldsymbol{y}) = \{\boldsymbol{\chi}_S(\widehat{\boldsymbol{x}}, \boldsymbol{y}) : \widehat{\boldsymbol{x}} \in S_{\text{ref}}\}.$$

## 3. ISOGEOMETRIC DISCRETIZATION OF RANDOM DOMAINS

**3.1. Fundamental Notions.** We review the basic notions of isogeometric analysis, restricting ourselves to spaces constructed via locally quasi-uniform  $p$ -open knot vectors, as required by the theory presented in [4, 5].

**Definition 1.** Let  $p$  and  $k$  with  $0 \leq p < k$ . A *locally quasi uniform  $p$ -open knot vector* is a tuple

$$\Xi = [\xi_0 = \dots = \xi_p \leq \dots \leq \xi_k = \dots = \xi_{k+p}] \in [0, 1]^{k+p+1}$$

with  $\xi_0 = 0$  and  $\xi_{k+p} = 1$  such that there exists a constant  $\theta \geq 1$  with  $\theta^{-1} \leq h_j \cdot h_{j+1}^{-1} \leq \theta$  for all  $p \leq j < k$ , where  $h_j := \xi_{j+1} - \xi_j$ . The B-spline basis  $\{b_j^p\}_{0 \leq j < k}$  is then recursively defined according to

$$b_j^p(x) = \begin{cases} \mathbb{1}_{[\xi_j, \xi_{j+1})} & \text{if } p = 0, \\ \frac{x - \xi_j}{\xi_{j+p} - \xi_j} b_j^{p-1}(x) + \frac{\xi_{j+p+1} - x}{\xi_{j+p+1} - \xi_{j+1}} b_{j+1}^{p-1}(x) & \text{else,} \end{cases}$$

where  $\mathbb{1}_A$  refers to the indicator function of the set  $A$ . The corresponding spline space is finally defined according to  $\mathbb{S}^p(\Xi) := \text{span}(\{b_j^p\}_{j < k})$ .

To obtain spline spaces in two spatial dimensions, we employ a tensor product construction. More precisely, for a tuple  $\Xi = (\Xi_1, \Xi_2)$  of knot vectors and polynomial degrees  $\mathbf{p} = (p_1, p_2)$ , we define the spaces

$$\mathbb{S}^{\mathbf{p}}(\Xi) := \mathbb{S}^{p_1}(\Xi_1) \otimes \mathbb{S}^{p_2}(\Xi_2).$$

Given knot vectors  $\Xi_1, \Xi_2$  with knots  $\xi_i^k < \xi_{i+1}^k$  for  $k = 1, 2$ , sets of the form  $[\xi_j^1, \xi_{j+1}^1] \times [\xi_j^2, \xi_{j+1}^2]$  will be called *elements*. We reserve the letter  $h$  for the maximal diameter of all elements. For further concepts and algorithmic realization of B-splines, we refer to [40] and the references therein.

**3.2. Isogeometric boundary representation.** We assume the usual isogeometric setting for the surface  $S_{\text{ref}}$  of the reference domain  $D_{\text{ref}}$ , i.e. denoting the unit square by  $\square := [0, 1]^2$ , we assume that the surface  $S_{\text{ref}}$  can be decomposed into several smooth *patches*

$$S_{\text{ref}} = \bigcup_{i=1}^M S_{\text{ref}}^{(i)}.$$

The intersection  $S_{\text{ref}}^{(i)} \cap S_{\text{ref}}^{(i')}$  consists at most of a common vertex or a common edge for  $i \neq i'$ . In particular, each patch  $S_{\text{ref}}^{(i)}$  is the image of an invertible NURBS mapping

$$(3.1) \quad \mathbf{s}_i: \square \rightarrow S_{\text{ref}}^{(i)} \quad \text{with} \quad S_{\text{ref}}^{(i)} = \mathbf{s}_i(\square) \quad \text{for } i = 1, 2, \dots, M,$$

where  $\mathbf{s}_i$  is of the form

$$\mathbf{s}_i(x, y) := \sum_{0=i_1}^{k_1} \sum_{0=i_2}^{k_2} \frac{\mathbf{c}_{i_1, i_2} b_{i_1}^{p_1}(x) b_{i_2}^{p_2}(y) w_{i_1, i_2}}{\sum_{j_1=0}^{k_1-1} \sum_{j_2=0}^{k_2-1} b_{j_1}^{p_1}(x) b_{j_2}^{p_2}(y) w_{j_1, j_2}}$$

for control points  $\mathbf{c}_{i_1, i_2} \in \mathbb{R}^3$  and weights  $w_{i_1, i_2} > 0$ . We shall further follow the common convention that parametrizations with a common edge coincide except for orientation.

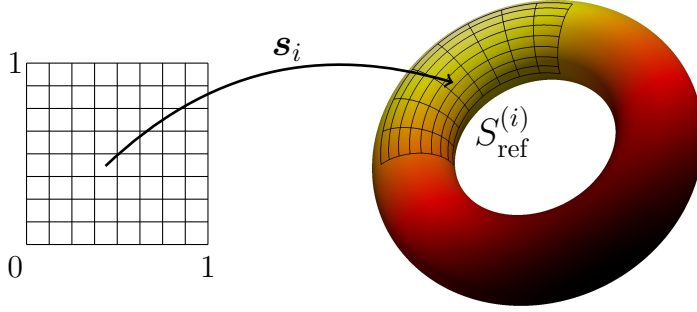


FIGURE 1. Surface representation and mesh generation.

Following the spirit of isogeometric analysis, the random surface  $S(\mathbf{y})$  from (2.8) is represented by the union of NURBS patches. This is achieved by appropriately discretizing the deformation field (2.6). More precisely, the random surface  $S(\mathbf{y})$  is discretized by  $S(\mathbf{y}) \approx S_h(\mathbf{y})$ , where the latter can be decomposed into  $M$  distinct NURBS patches

$$S_h(\mathbf{y}) = \bigcup_{i=1}^M S_h^{(i)}(\mathbf{y}).$$

Herein, the intersection  $S_h^{(i)}(\mathbf{y}) \cap S_h^{(i')}(\mathbf{y})$  again consists at most of a common vertex or a common edge for  $i \neq i'$  and each patch  $S_h^{(i)}(\mathbf{y})$  is given by the image of an invertible mapping

$$\mathbf{s}_{i,h}(\cdot, \mathbf{y}) : \square \rightarrow S^{(i)}(\mathbf{y}) \quad \text{with} \quad S^{(i)}(\mathbf{y}) = \mathbf{s}_{i,h}(\square, \mathbf{y}) \quad \text{for } i = 1, 2, \dots, M,$$

with

$$\mathbf{s}_{i,h}(\widehat{\mathbf{x}}, \mathbf{y}) = \chi_{S,h}|_i(\widehat{\mathbf{x}}, \mathbf{y}).$$

First, we note that  $\mathbf{s}_{i,h}(\widehat{\mathbf{x}}, \mathbf{y})$  is again a NURBS mapping if  $\chi_{S,h}|_i(\widehat{\mathbf{x}}, \mathbf{y})$  is discretized by using appropriate basis functions. In fact, if these basis functions are chosen also as NURBS, the randomness of the surface is encoded by transformations of the control points. Second, we note that  $\chi_S$  needs to be at least globally continuous to obtain an admissible surface transformation. Given a tuple of knot vectors  $\Xi$  and



polynomial degrees  $\mathbf{p}$ , a natural choice for the discretization of  $\chi_S(\cdot, \mathbf{y})$  is thus given by the vector valued spline space

$$\mathbf{S}_{\mathbf{p}, \Xi}(S_{\text{ref}}) = [\mathbf{S}_{\mathbf{p}, \Xi}(S_{\text{ref}})]^3$$

where

$$\mathbf{S}_{\mathbf{p}, \Xi}(S_{\text{ref}}) := \{f \in C(S_{\text{ref}}) : f|_i \circ \mathbf{s}_i \in \mathbf{S}_{\mathbf{p}}(\Xi) \text{ for } 1 \leq i \leq M\}.$$

Of course, the knot vectors and polynomial degrees could vary in each component and on each patch, but for simplicity we opt for using the same knots and degrees for better readability. Approximation properties for these spaces were derived in [5].

Next, we discuss how an approximation of  $\chi_{S,h}$  in terms of such basis functions can be derived by computing Karhunen-Loève expansion (2.6) of the underlying random deformation.

**3.3. Fast computation of the Karhunen-Loève expansion.** The computation of the Karhunen-Loève expansion of surface deformations from the expectation and the covariance amounts to the solution of the eigenvalue problem

$$\mathcal{C}_S \chi_{S,k} = \lambda_{S,k} \chi_{S,k}.$$

Based on the previous discussion, it is natural to choose a B-spline-based Galerkin discretization for the numerical solution of this eigenvalue problem. Hence, replacing  $[L^2(S_{\text{ref}})]^3$  by the B-spline space  $\mathbf{S}_{\mathbf{p}, \Xi}(S_{\text{ref}})$  in the eigenproblem's weak formulation

$$\text{Find } (\lambda_{S,k}, \chi_{S,k}) \in \mathbb{R} \times [L^2(S_{\text{ref}})]^3 \text{ such that}$$

$$(\mathcal{C}_S \chi_{S,k}, v)_{[L^2(S_{\text{ref}})]^3} = \lambda_{S,k} (\chi_{S,k}, v)_{[L^2(S_{\text{ref}})]^3} \text{ for all } v \in [L^2(S_{\text{ref}})]^3$$

yields the discrete generalized eigenvalue problem

$$(3.2) \quad \underline{\mathbf{C}} \underline{\chi}_k = \lambda_{k,h} \underline{\mathbf{M}} \underline{\chi}_k.$$

Although the mass matrix  $\underline{\mathbf{M}}$  is sparse, the covariance matrix  $\underline{\mathbf{C}}$  is typically densely populated, as it issues from the discretization of a nonlocal operator. Therefore, a naive solution of this eigenvalue problem is prohibitive for a larger number of degrees of freedom.

As a viable alternative, we assume that a low-rank factorization  $\underline{\mathbf{C}} \approx \underline{\mathbf{L}} \underline{\mathbf{L}}^\top$  of the covariance matrix is known. Such a factorization can, for example, efficiently be computed by the truncated pivoted Cholesky decomposition, see [28]. Inserting this decomposition into (3.2) yields

$$(3.3) \quad \underline{\mathbf{L}} \underline{\mathbf{L}}^\top \underline{\chi}_k = \lambda_{k,h} \underline{\mathbf{M}} \underline{\chi}_k.$$

Substituting  $\underline{\boldsymbol{\psi}}_k = \underline{\mathbf{M}}^{1/2} \underline{\boldsymbol{\chi}}_k$  therefore results in the eigenvalue problem

$$(3.4) \quad \underline{\mathbf{L}}^\top \underline{\mathbf{M}}^{-1} \underline{\mathbf{L}} \underline{\boldsymbol{\psi}}_k = \lambda_{k,h} \underline{\boldsymbol{\psi}}_k,$$

which has the same non-zero eigenvalues as (3.3), but is significantly smaller and cheaper to compute if  $\underline{\mathbf{C}}$  has low rank. The eigenvectors of (3.3) can be retrieved from (3.4) by making use of the relation  $\underline{\boldsymbol{\chi}}_k = \underline{\mathbf{M}}^{-1} \underline{\mathbf{L}} \underline{\boldsymbol{\psi}}_k$ .

*Remark 2.* Depending on the polynomial degrees  $\mathbf{p}$ , the supports of the basis functions in  $\mathbf{S}_{\mathbf{p},\Xi}(S_{\text{ref}})$  can be quite large. This renders the assembly of a single matrix entry as used for the truncated pivoted Cholesky decomposition computationally expensive. Therefore, we rather perform the Cholesky decomposition directly on the matrix  $\underline{\mathbf{C}}_\star$ , which is generated by the shape functions  $\mathbf{S}_{\mathbf{p},\Xi}^\star(S_{\text{ref}})$  of  $\mathbf{S}_{\mathbf{p},\Xi}(S_{\text{ref}})$ . Then, there exists a matrix version  $\underline{\mathbf{T}}$  representing the local-to-global map such that  $\underline{\mathbf{C}} = \underline{\mathbf{T}} \underline{\mathbf{C}}_\star \underline{\mathbf{T}}^\top$ . Now, substituting  $\underline{\mathbf{C}}_\star \approx \underline{\mathbf{L}}_\star \underline{\mathbf{L}}_\star^\top$  yields the low-rank factorization

$$\underline{\mathbf{C}} \approx \underline{\mathbf{T}} \underline{\mathbf{L}}_\star (\underline{\mathbf{T}} \underline{\mathbf{L}}_\star)^\top = \underline{\mathbf{L}} \underline{\mathbf{L}}^\top.$$

## 4. BOUNDARY INTEGRAL EQUATIONS

**4.1. Computing the scattered wave.** We recall the solution of the boundary value problem (1.1) by means of boundary integral equations. To this end, and for sake of simplicity in representation, we assume for the moment that the domain  $D$  is fixed and has a Lipschitz surface  $S = \partial D$ .

We introduce the acoustic single layer operator

$$\mathcal{V}: H^{-1/2}(S) \rightarrow H^{1/2}(S), \quad (\mathcal{V}\rho)(\mathbf{x}) := \int_S \Phi(\mathbf{x}, \mathbf{z}) \rho(\mathbf{z}) \, d\sigma_{\mathbf{z}},$$

and the acoustic double layer operator

$$\mathcal{K}: L^2(S) \rightarrow L^2(S), \quad (\mathcal{K}\rho)(\mathbf{x}) := \int_S \frac{\partial \Phi(\mathbf{x}, \mathbf{z})}{\partial \mathbf{n}_{\mathbf{z}}} \rho(\mathbf{z}) \, d\sigma_{\mathbf{z}}.$$

Here,  $\mathbf{n}_{\mathbf{z}}$  denotes the outward pointing normal vector at the surface point  $\mathbf{z} \in S$ , while  $\Phi(\cdot, \cdot)$  denotes the Green's function for the Helmholtz equation. In three spatial dimensions, the Green's function is given by

$$\Phi(\mathbf{x}, \mathbf{z}) = \frac{e^{i\kappa \|\mathbf{x} - \mathbf{z}\|_2}}{4\pi \|\mathbf{x} - \mathbf{z}\|_2}.$$

Considering an incident plane wave  $u_{\text{inc}}(\mathbf{x}) = e^{i\kappa \langle \mathbf{d}, \mathbf{x} \rangle}$ ,  $\|\mathbf{d}\|_2 = 1$ , the Neumann data of the total wave  $u = u_{\text{inc}} + u_s$  at the surface  $S$  can be determined by the boundary

integral equation

$$(4.1) \quad \left( \frac{1}{2} + \mathcal{K}^* - i\eta\mathcal{V} \right) \frac{\partial u}{\partial \mathbf{n}} = \frac{\partial u_{\text{inc}}}{\partial \mathbf{n}} - i\eta u_{\text{inc}} \quad \text{on } S,$$

with  $\eta = \kappa/2$ , compare to [8].

From the Cauchy data of  $u$  at  $S$ , we can determine the scattered wave  $u_s$  in any point in the exterior of the obstacle by applying the potential evaluation

$$(4.2) \quad u_s(\mathbf{x}) = \int_S \Phi(\mathbf{x}, \mathbf{z}) \frac{\partial u}{\partial \mathbf{n}_z}(\mathbf{z}) \, d\sigma_z, \quad \mathbf{x} \in \mathbb{R}^3 \setminus \bar{D}.$$

**4.2. Scattered wave representation at an artificial interface.** We introduce an artificial interface  $T \subset \mathbb{R}^3$ , being sufficiently large to guarantee that  $T$  encloses all realizations of the domain  $D$ . In view of (4.2), we may compute the Cauchy data  $u_s|_T$  and  $(\partial u_s / \partial \mathbf{n})|_T$  of the scattered wave at the artificial interface  $T$ . **Taking the normal derivative of (4.2) at  $T$  yields**

$$\frac{\partial u_s}{\partial \mathbf{n}_x}(\mathbf{x}) = \int_S \frac{\partial \Phi(\mathbf{x}, \mathbf{z})}{\partial \mathbf{n}_x} \frac{\partial u}{\partial \mathbf{n}_z}(\mathbf{z}) \, d\sigma_z, \quad \mathbf{x} \in T.$$

For any  $\mathbf{x} \in \mathbb{R}^3$  located outside the artificial interface, we may now either employ the representation formula (4.2) **for  $T$  rather than for  $S$**  or the representation formula

$$(4.3) \quad u_s(\mathbf{x}) = \int_T \left\{ \frac{\partial \Phi(\mathbf{x}, \mathbf{z})}{\partial \mathbf{n}_z} u_s(\mathbf{z}) - \Phi(\mathbf{x}, \mathbf{z}) \frac{\partial u_s}{\partial \mathbf{n}_z}(\mathbf{z}) \right\} \, d\sigma_z$$

to compute the scattered wave  $u_s$ , **see [8]**.

The major advantage of (4.3) over (4.2) is that the artificial interface is fixed in contrast to the shape of the random obstacle later on.

**4.3. Scattering at random obstacles.** From now on, let the obstacle be subject to uncertainty as introduced in Section 2. We describe the uncertain obstacle  $D = D(\mathbf{y})$  by its random surface  $S(\mathbf{y})$ , which is given by (2.8).

Having the incident wave  $u_{\text{inc}}$  at hand, the boundary value problem for the total field  $u(\mathbf{y}) = u_s(\mathbf{y}) + u_{\text{inc}}$  for any  $\mathbf{y} \in \Gamma$  reads

$$(4.4) \quad \begin{aligned} \Delta u(\mathbf{y}) + \kappa^2 u(\mathbf{y}) &= 0 \quad \text{in } \mathbb{R}^3 \setminus \overline{D(\mathbf{y})}, \\ u(\mathbf{y}) &= 0 \quad \text{on } S(\mathbf{y}), \\ \sqrt{r} \left( \frac{\partial u_s}{\partial r} - i\kappa u_s \right) &\rightarrow 0 \quad \text{as } r = \|\mathbf{x}\|_2 \rightarrow \infty. \end{aligned}$$

By the construction of  $S(\mathbf{y})$ , the random scattering problem (4.4) exhibits a unique solution for each realization  $\mathbf{y} \in \Gamma$  of the random parameter. Moreover, it has

been shown in [34] for the case of the Helmholtz transmission problem that the total wave  $u(\mathbf{y})$  exhibits an analytic extension into a certain region of the complex plane with respect to the parameter  $\mathbf{y} \in \Gamma$ . This particularly allows for the use of higher order quadrature methods, like quasi-Monte Carlo methods, see e.g. [6, 39], or even sparse quadrature methods, see e.g. [23, 34] in order to compute quantities of interest, such as expectation and variance. Extensions to the Maxwell case are discussed in [1, 36, 37].

**4.4. Expectation of the scattered wave.** The scattered wave's expectation can be computed for any given point  $\mathbf{x} \in \mathbb{R}^3$  by the representation formula (4.2), which leads to

$$(4.5) \quad \mathbb{E}[u_s](\mathbf{x}) = \mathbb{E} \left[ \int_{S(\mathbf{y})} \Phi(\mathbf{x}, \mathbf{z}) \frac{\partial u_s}{\partial \mathbf{n}_z}(\mathbf{z}, \cdot) d\sigma_z \right].$$

Obviously, (4.5) only makes sense if  $\mathbf{x} \in \mathbb{R}^3$  is sufficiently far away from the random obstacle. Otherwise, there might be instances  $\mathbf{y} \in \Gamma$  such that  $\mathbf{x} \in D(\mathbf{y})$ , i.e. the point  $\mathbf{x} \in \mathbb{R}^3$  does not lie outside the obstacle almost surely.

If the expectation needs to be evaluated at many locations, it is much more efficient to introduce the artificial interface  $T$  and to consider expression (4.3). For any  $\mathbf{x} \in \mathbb{R}^3$  lying outside the interface  $T$ , it holds

$$(4.6) \quad \mathbb{E}[u_s](\mathbf{x}) = \int_T \left\{ \Phi(\mathbf{x}, \mathbf{z}) \mathbb{E} \left[ \frac{\partial u_s}{\partial \mathbf{n}_z} \right](\mathbf{z}) - \frac{\partial \Phi(\mathbf{x}, \mathbf{z})}{\partial \mathbf{n}_z} \mathbb{E}[u_s](\mathbf{z}) \right\} d\sigma_z.$$

As a consequence, the scattered wave's expectation is completely encoded in the Cauchy data at the artificial interface  $T$ . This means that we only need to compute the expected Cauchy data

$$(4.7) \quad \mathbb{E}[u_s](\mathbf{x}) = \int_{\Gamma} \left\{ \int_{S(\mathbf{y})} \Phi(\mathbf{x}, \mathbf{z}) \frac{\partial u}{\partial \mathbf{n}}(\mathbf{z}, \mathbf{y}) d\sigma_z \right\} d\mu(\mathbf{y})$$

and

$$(4.8) \quad \mathbb{E} \left[ \frac{\partial u_s}{\partial \mathbf{n}_x} \right](\mathbf{x}) = \int_{\Gamma} \left\{ \int_{S(\mathbf{y})} \frac{\Phi(\mathbf{x}, \mathbf{z})}{\partial \mathbf{n}_z} u(\mathbf{z}, \mathbf{y}) d\sigma_z \right\} d\mu(\mathbf{y})$$

of the scattered wave at the artificial interface  $T$ , which is of lower spatial dimension than the exterior domain. **Here,  $\mu$  is the joint probability measure of the random variables  $\mathbf{y}$  coming from the Karhunen-Loève expansion (2.7).**

**4.5. Variance of the scattered wave.** The variance  $\mathbb{V}[u_s]$  of the scattered wave  $u_s(\mathbf{x})$  at a point  $\mathbf{x} \in \mathbb{R}^3$  outside the artificial interface  $T$  depends nonlinearly on the Cauchy data of  $u_s$  at the interface. Nonetheless, we can make use of the fact that the variance is the trace –in the algebraic sense– of the covariance, i.e.

$$(4.9) \quad \mathbb{V}[u_s](\mathbf{x}) = \text{Cov}[u_s](\mathbf{x}, \mathbf{x}') \Big|_{\mathbf{x}=\mathbf{x}'} = \text{Cor}[u_s](\mathbf{x}, \mathbf{x}') \Big|_{\mathbf{x}=\mathbf{x}'} - |\mathbb{E}[u_s](\mathbf{x})|^2,$$

where the covariance is given by

$$\begin{aligned} \text{Cov}[u_s](\mathbf{x}, \mathbf{x}') &= \mathbb{E} \left[ \left( u_s(\mathbf{x}, \cdot) - \mathbb{E}[u_s](\mathbf{x}) \right) \overline{\left( u_s(\mathbf{x}', \cdot) - \mathbb{E}[u_s](\mathbf{x}') \right)} \right] \\ &= \mathbb{E} \left[ u_s(\mathbf{x}, \cdot) \overline{u_s(\mathbf{x}', \cdot)} \right] - \mathbb{E}[u_s](\mathbf{x}) \overline{\mathbb{E}[u_s](\mathbf{x}')}. \end{aligned}$$

Hence, it holds for the correlation

$$\text{Cor}[u_s](\mathbf{x}, \mathbf{x}') = \mathbb{E} \left[ u_s(\mathbf{x}, \cdot) \overline{u_s(\mathbf{x}', \cdot)} \right].$$

The correlation is a higher-dimensional object which depends only linearly on the second moment of the Cauchy data of the scattered wave at the artificial interface  $T$ . This greatly simplifies the computation of the variance. More precisely, by defining for  $\mathbf{x}, \mathbf{x}' \in T$  the correlations

$$\begin{aligned} \text{Cor}[u_s](\mathbf{x}, \mathbf{x}') &:= \mathbb{E} \left[ \left( \int_{S(\mathbf{y})} \Phi(\mathbf{x}, \mathbf{z}) \frac{\partial u_s}{\partial \mathbf{n}_z}(\mathbf{z}, \mathbf{y}) \, d\sigma_z \right) \overline{\left( \int_{S(\mathbf{y})} \Phi(\mathbf{x}', \mathbf{z}) \frac{\partial u_s}{\partial \mathbf{n}_z}(\mathbf{z}, \mathbf{y}) \, d\sigma_z \right)} \right], \\ \text{Cor} \left[ \frac{\partial u_s}{\partial \mathbf{n}} \right](\mathbf{x}, \mathbf{x}') &:= \mathbb{E} \left[ \left( \int_{S(\mathbf{y})} \frac{\partial \Phi(\mathbf{x}, \mathbf{z})}{\partial \mathbf{n}_z} u_s(\mathbf{z}, \mathbf{y}) \, d\sigma_z \right) \overline{\left( \int_{S(\mathbf{y})} \frac{\partial \Phi(\mathbf{x}', \mathbf{z})}{\partial \mathbf{n}_z} u_s(\mathbf{z}, \mathbf{y}) \, d\sigma_z \right)} \right], \end{aligned}$$

and

$$\begin{aligned} \text{Cor} \left[ u_s, \frac{\partial u_s}{\partial \mathbf{n}} \right](\mathbf{x}, \mathbf{x}') &= \overline{\text{Cor} \left[ \frac{\partial u_s}{\partial \mathbf{n}}, u_s \right](\mathbf{x}', \mathbf{x})} \\ &:= \mathbb{E} \left[ \overline{\left( \int_{S(\mathbf{y})} \Phi(\mathbf{x}, \mathbf{z}) \frac{\partial u_s}{\partial \mathbf{n}_z}(\mathbf{z}, \omega) \, d\sigma_z \right)} \left( \int_{S(\mathbf{y})} \frac{\partial \Phi(\mathbf{x}', \mathbf{z})}{\partial \mathbf{n}_z} u_s(\mathbf{z}, \mathbf{y}) \, d\sigma_z \right) \right], \end{aligned}$$

we find for two points  $\mathbf{x}, \mathbf{x}' \in \mathbb{R}^3$  lying outside of the interface  $T$  the deterministic expression

$$(4.10) \quad \begin{aligned} \text{Cor}[u_s](\mathbf{x}, \mathbf{x}') &= \int_T \int_T \left\{ \Phi(\mathbf{x}, \mathbf{z}) \overline{\Phi(\mathbf{x}', \mathbf{z}')} \text{Cor} \left[ \frac{\partial u_s}{\partial \mathbf{n}} \right](\mathbf{z}, \mathbf{z}') \right. \\ &\quad - \Phi(\mathbf{x}, \mathbf{z}) \frac{\overline{\partial \Phi(\mathbf{x}', \mathbf{z}')}}{\partial \mathbf{n}_{z'}} \text{Cor} \left[ \frac{\partial u_s}{\partial \mathbf{n}}, u_s \right](\mathbf{z}, \mathbf{z}') \\ &\quad - \frac{\partial \Phi(\mathbf{x}, \mathbf{z})}{\partial \mathbf{n}_z} \overline{\Phi(\mathbf{x}', \mathbf{z}')} \text{Cor} \left[ u_s, \frac{\partial u_s}{\partial \mathbf{n}} \right](\mathbf{z}, \mathbf{z}') \\ &\quad \left. + \frac{\partial \Phi(\mathbf{x}, \mathbf{z})}{\partial \mathbf{n}_z} \frac{\overline{\partial \Phi(\mathbf{x}', \mathbf{z}')}}{\partial \mathbf{n}_{z'}} \text{Cor}[u_s](\mathbf{z}, \mathbf{z}') \right\} d\sigma_{z'} d\sigma_z. \end{aligned}$$

## 5. MULTILEVEL QUADRATURE

In order to calculate quantities of interest efficiently, we employ a multilevel quadrature approach. For the computation of the expectation, we may exploit the linearity of the expectation in formula (4.6) and rely on the Cauchy data on the spatial refinement levels  $\ell = 0, 1, \dots, L$  computed at the artificial interface  $T$ . Thus, we obtain

$$(5.1) \quad \mathbb{E}[u_s](\mathbf{x}) \approx \int_T \left\{ \Phi(\mathbf{x}, \mathbf{z}) \mathcal{Q}_L^{\text{ML}} \left[ \frac{\partial u_s}{\partial \mathbf{n}_z} \right](\mathbf{z}) + \frac{\partial \Phi(\mathbf{x}, \mathbf{z})}{\partial \mathbf{n}_z} \mathcal{Q}_L^{\text{ML}}[u_s](\mathbf{z}) \right\} d\sigma_z$$

with

$$\mathcal{Q}_L^{\text{ML}}[\rho](\mathbf{z}) := \sum_{\ell=0}^L \mathcal{Q}_{L-\ell}(\rho^{(\ell)}(\mathbf{z}, \cdot) - \rho^{(\ell-1)}(\mathbf{z}, \cdot)) \quad \text{for } \mathbf{z} \in T,$$

where  $\mathcal{Q}_\ell$  is a quadrature rule on level  $\ell$ . Moreover, the function  $\rho^{(\ell)}$  is the Galerkin projection of the density  $\rho$  evaluated at the artificial interface for the spatial refinement on level  $\ell$  of the scatterer, where we set  $\rho^{(-1)} \equiv 0$ .

For the approximation error of the multilevel quadrature, there holds a sparse tensor product-like error estimate. If  $\varepsilon_\ell \rightarrow 0$  is a monotonically decreasing sequence with  $\varepsilon_\ell \cdot \varepsilon_{L-\ell} = \varepsilon_L$  for every  $L \in \mathbb{N}$  and

$$\|\mathcal{Q}_{L-\ell}\rho - \mathbb{E}[\rho]\| \leq c_1 \varepsilon_{L-\ell} \quad \text{and} \quad \|\rho^{(\ell)} - \rho\| \leq c_2 \varepsilon_\ell$$

for some suitable norms and constants  $c_1, c_2 > 0$ , then

$$\|\mathcal{Q}_L^{\text{ML}}[\rho] - \mathbb{E}[\rho]\| \leq CL\varepsilon_L$$

for a constant  $C > 0$ , **given that  $\rho$  is sufficiently regular**. We refer to [29] for **details on the multilevel quadrature** and to [31] for **the required mixed regularity estimates**.

For the calculation of the variance, we employ formula (4.10) and obtain

$$\begin{aligned} \text{Cor}[u_s](\mathbf{x}, \mathbf{x}') \approx & \int_T \int_T \left\{ \Phi(\mathbf{x}, \mathbf{z}) \overline{\Phi(\mathbf{x}', \mathbf{z}')} \mathcal{Q}_L^{\text{ML}} \left[ \frac{\partial u_s}{\partial \mathbf{n}_z} \otimes \frac{\partial u_s}{\partial \mathbf{n}_{z'}} \right](\mathbf{z}, \mathbf{z}') \right. \\ & - \Phi(\mathbf{x}, \mathbf{z}) \frac{\overline{\partial \Phi(\mathbf{x}', \mathbf{z}')}}{\partial \mathbf{n}_{z'}} \mathcal{Q}_L^{\text{ML}} \left[ \frac{\partial u_s}{\partial \mathbf{n}_z} \otimes u_s \right](\mathbf{z}, \mathbf{z}') \\ & - \frac{\partial \Phi(\mathbf{x}, \mathbf{z})}{\partial \mathbf{n}_z} \overline{\Phi(\mathbf{x}', \mathbf{z}')} \mathcal{Q}_L^{\text{ML}} \left[ u_s \otimes \frac{\partial u_s}{\partial \mathbf{n}_{z'}} \right](\mathbf{z}, \mathbf{z}') \\ & \left. + \frac{\partial \Phi(\mathbf{x}, \mathbf{z})}{\partial \mathbf{n}_z} \frac{\overline{\partial \Phi(\mathbf{x}', \mathbf{z}')}}{\partial \mathbf{n}_{z'}} \mathcal{Q}_L^{\text{ML}}[u_s \otimes u_s](\mathbf{z}, \mathbf{z}') \right\} d\sigma_{z'} d\sigma_z \end{aligned}$$

with

$$\mathcal{Q}_L^{\text{ML}}[\rho \otimes \mu](\mathbf{z}, \mathbf{z}') := \sum_{\ell=0}^L \mathcal{Q}_{L-\ell}((\rho \otimes \mu)^{(\ell)}(\mathbf{z}, \mathbf{z}', \cdot) - (\rho \otimes \mu)^{(\ell-1)}(\mathbf{z}, \mathbf{z}', \cdot)),$$

where  $(\rho \otimes \mu)^{(\ell)} := \rho^{(\ell)} \otimes \mu^{(\ell)}$ . In principle, it would also be possible to opt for the multi-index quadrature, which has been proposed in [2] for the computation of higher order moments. In this case, one ends up with

$$(\rho \otimes \mu)^{(\ell)}(\mathbf{z}, \mathbf{z}', \mathbf{y}) := \sum_{j=0}^{\ell} \rho^{(\ell-j)}(\mathbf{z}, \mathbf{y}) \mu^{(j)}(\mathbf{z}', \mathbf{y}) = \sum_{j=0}^{\ell} \rho^{(j)}(\mathbf{z}, \mathbf{y}) \mu^{(\ell-j)}(\mathbf{z}', \mathbf{y}).$$

Finally, we remark that there holds a similar error estimate as for the expectation and that isogeometric analysis was recently combined with a multi-index quadrature in [3].

## 6. BAYESIAN SHAPE INVERSION

Let  $\mathcal{A}(\mathbf{y}): H^1(S(\mathbf{y})) \rightarrow C(T)$ ,  $\mathbf{y} \in \Gamma$ , be the solution operator which maps the incident wave at  $S(\mathbf{y})$  to the scattered wave at  $T$ . Fixing the incident wave  $u_{\text{inc}}$ , we denote by

$$G: \Gamma \rightarrow C(T), \quad \mathbf{y} \mapsto u_s(\mathbf{y})$$

the uncertainty-to-solution map.

In forward uncertainty quantification, the goal is to compute quantities of interest  $\text{QoI}(u_s)$ , with respect to the prior measure  $\mu_0$ , which is induced by the random variables from (2.6). Often, quantities of interest are assumed to be linear functionals. The goal of Bayesian inversion as introduced in [9] is to incorporate noisy measurements of solutions  $\mathcal{A}(\mathbf{y})u_{\text{inc}}$ , after potentially incomplete observations. This is modelled by first considering a bounded, linear observation operator  $O: C(T) \rightarrow \mathbb{C}^N$ , which **performs** point measurements of the scattered wave at the artificial interface  $T$ . Combining the solution operator with the observation **operator** yields the uncertainty-to-observation mapping

$$(6.1) \quad \mathcal{G}: \Gamma \rightarrow \mathbb{C}^N, \quad \mathbf{y} \mapsto \mathcal{G}(\mathbf{y}) = O(\mathcal{A}(\mathbf{y})u_{\text{inc}}).$$

The measured data  $\boldsymbol{\delta}$  is modelled as resulting from an observation by  $O$ , perturbed by additive Gaussian noise according to

$$\boldsymbol{\delta} = \mathcal{G}(\mathbf{y}^*) + \boldsymbol{\eta},$$

where  $\mathbf{y}^*$  is the unknown, exact parameter. We assume that the noise  $\boldsymbol{\eta}$  is given by a complex, circular, symmetric Gaussian random vector with symmetric, positive definite covariance matrix  $\boldsymbol{\Sigma} \in \mathbb{R}^{N \times N}$ , i.e.  $\boldsymbol{\eta} \sim \mathcal{CN}(0, \boldsymbol{\Sigma})$ . Note that this is equivalent to  $\boldsymbol{\eta} = \boldsymbol{\eta}_r + i\boldsymbol{\eta}_i$  with **independent**  $\boldsymbol{\eta}_r$ ,  $\boldsymbol{\eta}_i$  and  $\boldsymbol{\eta}_r, \boldsymbol{\eta}_i \sim \mathcal{N}(0, \boldsymbol{\Sigma}/2)$ , and respects the physical time-harmonic model of the scattering problem, see [46].

Within this article, we aim at predicting the shape of the random scatterer based on observations of  $u_s$  at  $T$ . Concretely, we wish to compute expectation and variance of the deformation field. To that end, we define the Gaussian potential, also referred to as the least-squares or data misfit functional, by  $\Phi_{\Sigma} : \Gamma \times \mathbb{C}^N \rightarrow \mathbb{R}$ ,

$$(6.2) \quad \Phi_{\Sigma}(\mathbf{y}, \boldsymbol{\delta}) := \frac{1}{2} \|\boldsymbol{\delta} - \mathcal{G}(\mathbf{y})\|_{\Sigma^{-1}}^2 := \frac{1}{2} (\boldsymbol{\delta} - \mathcal{G}(\mathbf{y}))^{\top} \Sigma^{-1} (\boldsymbol{\delta} - \mathcal{G}(\mathbf{y})).$$

Given the prior measure  $\mu_0$ , Bayes' formula yields an expression for the posterior measure  $\mu^{\delta}$  on  $\Gamma$ , given the data  $\boldsymbol{\delta}$  with the Radon-Nikodym derivative is given by

$$\frac{d\mu^{\delta}}{d\mu_0}(\mathbf{y}) = \frac{e^{-\Phi_{\Sigma}(\mathbf{y}, \boldsymbol{\delta})}}{Z}$$

with

$$Z := \int_{\Gamma} e^{-\Phi_{\Sigma}(\mathbf{y}, \boldsymbol{\delta})} \mu_0(d\mathbf{y}) > 0,$$

see [9].

Now, the expected shape of the random scatterer is given by

$$\mathbb{E}^{\mu^{\delta}}[\boldsymbol{\chi}](\hat{\mathbf{x}}) := \int_{\Gamma} \boldsymbol{\chi}(\hat{\mathbf{x}}, \mathbf{y}) \frac{e^{-\Phi_{\Sigma}(\mathbf{y}, \boldsymbol{\delta})}}{Z} d\mu_0(\mathbf{y}), \quad \hat{\mathbf{x}} \in S_{\text{ref}},$$

and its variance for  $\hat{\mathbf{x}} \in S_{\text{ref}}$  by

$$\mathbb{V}^{\mu^{\delta}}[\boldsymbol{\chi}](\hat{\mathbf{x}}) := \int_{\Gamma} \boldsymbol{\chi}(\hat{\mathbf{x}}, \mathbf{y}) \boldsymbol{\chi}(\hat{\mathbf{x}}, \mathbf{y})^{\top} \frac{e^{-\Phi_{\Sigma}(\mathbf{y}, \boldsymbol{\delta})}}{Z} d\mu_0(\mathbf{y}) - \mathbb{E}^{\mu^{\delta}}[\boldsymbol{\chi}](\hat{\mathbf{x}}) \mathbb{E}^{\mu^{\delta}}[\boldsymbol{\chi}](\hat{\mathbf{x}})^{\top}.$$

In order to approximate these integrals numerically, we shall employ the multilevel ratio estimator, which splits the computation of the actual integral and the normalization constant and approximates each by a telescoping sum, see [10] and the references therein. For the normalization constant, we consider

$$\mathcal{Q}_L^{\text{ML}}[\rho] := \sum_{\ell=0}^L \mathcal{Q}_{L-\ell}(\rho_{\ell} - \rho_{\ell-1})$$

with

$$\rho_{\ell} := e^{-\Phi_{\Sigma, \ell}(\mathbf{y}, \boldsymbol{\delta})}, \quad \Phi_{\Sigma, \ell}(\mathbf{y}, \boldsymbol{\delta}) := \frac{1}{2} \|\boldsymbol{\delta} - \mathcal{O}(\mathcal{A}_{\ell}(\mathbf{y})u_{\text{inc}})\|_{\Sigma^{-1}}^2, \quad Z_{-1} := 0,$$

i.e. we consider a multilevel hierarchy based on approximations of the scattered wave on different levels of refinement. Now, we may compute, for example, the expected deformation field according to

$$\mathcal{Q}_L^{\text{ML}, \mu^{\delta}}[\boldsymbol{\chi}] := \left( \sum_{\ell=0}^L \mathcal{Q}_{L-\ell}(\boldsymbol{\chi} \cdot (\rho_{\ell} - \rho_{\ell-1})) \right) / \mathcal{Q}_L^{\text{ML}}[\rho].$$



We remark that Bayesian inversion employing the ratio estimator approximated by quasi-Monte Carlo and its multilevel variants may fail to converge for concentrated a posteriori measures. To tackle this, suitable remedies based on Markov Chain Monte Carlo or Laplace approximations have been devised [41, 42], which can be directly employed in the current setting but that we forgo for the sake of brevity.

## 7. NUMERICAL EXAMPLES

**7.1. Geometries, discretization, and multilevel quadrature.** We consider a scatterer  $D_{\text{ref}}$  given by a cuboid  $[0, 3] \times [0, 2] \times [0, 1]$  with six drilled holes, with an artificial interface  $T$  given by the cuboid  $[-2, 5] \times [-2, 4] \times [-2, 3]$ . A visualization of the situation may be found in Figure 7.2. The surface of the scatterer is represented by 82 patches and the artificial interface by 52 patches. The wavenumber is chosen as  $\kappa = 1$ .

We discretize the random field with globally continuous B-splines of polynomial degree  $p = 2$  in each spatial variable and uniform three spatial refinements, leading to a dense covariance matrix  $\underline{\mathbf{C}} \in \mathbb{R}^{19\,896 \times 19\,896}$ . For an efficient computation of the Karhunen-Loève expansion, we proceed as outlined in Remark 2. The artificial interface is discretized with tensor-product polynomials of degree  $p = 6$  on each patch. The Cauchy data on the artificial interface can then be obtained from the values on  $52 \cdot 7^2 = 2\,548$  point evaluations on the interface by solving 52 local interpolation problems of size  $7^2$ .

For the application of the multilevel quadrature, we perform the acoustic scattering computations with patchwise continuous B-splines of degree  $p = 0, 1, 2$  and the refinement levels  $\ell = 0, 1, \dots, 4 - p$ , leading to the number of degrees of freedom tabulated in Table 1.

	$\ell = 0$	$\ell = 1$	$\ell = 2$	$\ell = 3$	$\ell = 4$
$p = 0$	82	328	1 312	5 248	20 992
$p = 1$	328	738	2 050	6 642	—
$p = 2$	738	1 312	2 952	—	—

TABLE 1. Number of degrees of freedom of the boundary element solver for different polynomial degrees  $p$  and refinement levels  $\ell$ .

The implementation of the spatial discretizations is based on the C++ library `bembe1` [12, 13], which is easily adapted to our needs and provides fast compression schemes for the scattering computations.

The multilevel quadrature is either based on a quasi-Monte Carlo quadrature using the Halton sequence, see [6], or on the anisotropic sparse grid quadrature using Gauß-Legendre points as described in [23]. The latter is available as open source software package SPQR<sup>1</sup>. Due to the high asymptotic convergence rate of  $h^{2p+2}$  of the higher-order method for the scattering computations, the number of samples for the multilevel quadrature has to be adapted for each level according to  $\sim h^{-2p-2}$  for the quasi-Monte Carlo quadrature (QMC) and according to the error estimates in [24] for the sparse grid quadrature (SG). This yields the number of quadrature points as shown in Table 2.

		$\ell = 0$	$\ell = 1$	$\ell = 2$	$\ell = 3$	$\ell = 4$
$p = 0$	QMC	4 096	1 024	256	64	16
	SG	52 509	12 017	2 513	471	61
$p = 1$	QMC	65 536	4 096	256	16	—
	SG	809 881	52 509	2 513	61	—
$p = 2$	QMC	65 536	1 024	16	—	—
	SG	809 881	12 017	61	—	—

TABLE 2. Number of samples on the different levels for SG and QMC.

Due to the large number of samples and the high computational costs of solving three dimensional scattering problems, we employ a hybrid parallelization with MPI and OpenMP to accelerate the sampling process. The computations have been carried out with a combined hybrid parallelization with MPI and OpenMP on a total of 192 cores. Therein,  $2^\ell$  OpenMP threads have been dedicated to the boundary element solver on level  $\ell$ , while the MPI processes were used to parallelize the sampling of the random parameter. The computations have been carried out on a compute cluster with four nodes equipped with a Intel(R) Xeon(R) Platinum 8268 CPU 2.90GHz processor each (hyperthreading enabled). The runtimes for a single run of the boundary element solver in this setting are tabulated in Table 3. It is evident from these timings that the use of a single level Monte Carlo method for the computation of a reference solution with  $10^5$  or more samples is out of reach with the available resources.

<sup>1</sup><https://github.com/muchip/SPQR>

	$\ell = 0$	$\ell = 1$	$\ell = 2$	$\ell = 3$	$\ell = 4$
threads	1	2	4	8	16
$p = 0$	0.312	8.6	61.1	125	339
$p = 1$	0.838	14.2	91.6	221	—
$p = 2$	2.2	21.5	146	—	—

TABLE 3. Runtimes in seconds of a single run of the boundary element solver on the given number of threads.

**7.2. Forward problem.** In the following, we consider domain deformations with identity expectation  $\mathbb{E}[\chi](\hat{\mathbf{x}}) = \hat{\mathbf{x}}$  and the covariance function given by

$$\text{Cov}[\chi_S](\mathbf{x}, \mathbf{y}) = \begin{bmatrix} \frac{1}{10} e^{-\frac{\|\mathbf{x}-\mathbf{y}\|_2^2}{2 \cdot 16^2}} & 0 & \frac{1}{10^6} e^{-\frac{\|\mathbf{x}-\mathbf{y}\|_2^2}{2 \cdot 64^2}} \\ 0 & \frac{1}{10} e^{-\frac{\|\mathbf{x}-\mathbf{y}\|_2^2}{2 \cdot 4^2}} & 0 \\ \frac{1}{10^6} e^{-\frac{\|\mathbf{x}-\mathbf{y}\|_2^2}{2 \cdot 64^2}} & 0 & \frac{1}{5} e^{-\frac{\|\mathbf{x}-\mathbf{y}\|_2^2}{2}} \end{bmatrix}.$$

Four different realizations of the deformed scatterer and corresponding scattered waves at the artificial interface are illustrated in Figure 7.2. The singular values of the corresponding deformation field are illustrated in Figure 3. The Karhunen-Loève expansion is truncated after  $K = 134$  terms.

For demonstrating the validity of the dimension reduction via the artificial interface, we also define 100 evaluation points outside of the artificial interface, which are equally distributed on a sphere centered around the origin with radius  $r = 8$ . Note that the origin is one of the corners of the reference geometry.

In order to measure approximation errors, we compare the solutions obtained by the multilevel SG to that of the multilevel QMC on the finest level and vice versa. The error is given in terms of the  $\ell^\infty$ -error computed with respect to the respective evaluation points. The results for the expectation are illustrated in Figure 4. The dashed curves indicate the convergence of the spatial approximation on the reference domain. The corresponding results for the correlation can be found in Figure 5.

**7.3. Shape inversion.** For illustrating the Bayesian shape inversion, we pick a realization of the random domain perturbation described by the parameter  $\mathbf{y}^* \in \Gamma$  from the model presented in the previous subsection and consider it to be our reference solution. The measurement operator  $O$  defining  $\mathcal{G}$  is given by point evaluations of the scattered wave in the midpoints of the 52 patches at the artificial interface. The noise level is set to  $\Sigma = \sigma^2 \mathbf{I}$ , where  $\sigma = 0.1 \cdot \max |\mathcal{G}(\mathbf{y}^*)|$ . The prior is set to  $d\mu(\mathbf{y}) = d\mathbf{y}/2^K$ , with  $K$  being the dimension of the parameter space, yielding the

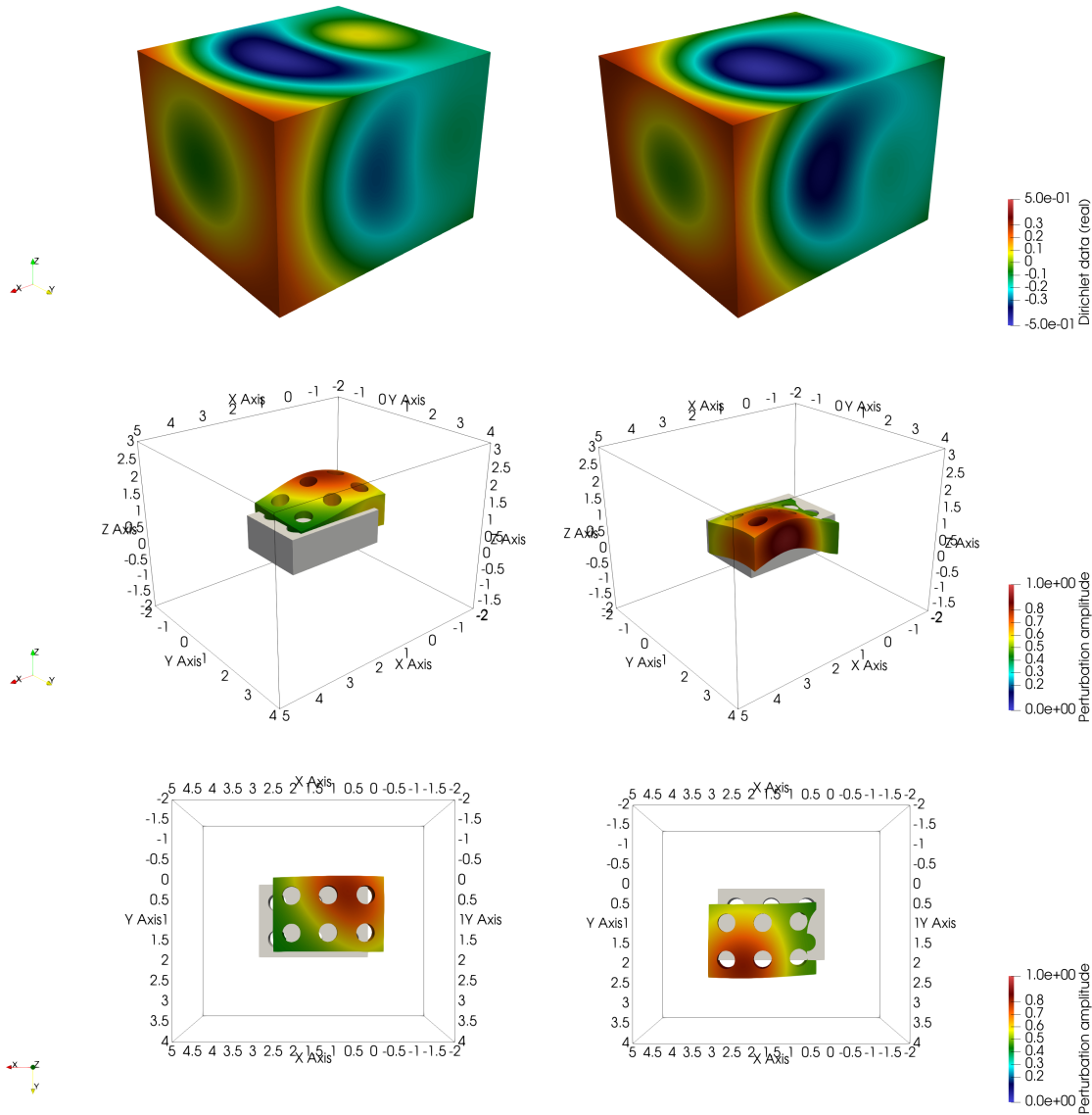


FIGURE 2. Domain perturbations drawn from the random field and scattered wave on the artificial interface.

unperturbed domain to be the prior expectation. Figure 6 illustrates the reference solution, the prior and posterior expectation and the posterior's  $2\sigma$  confidence region in each coordinate direction obtained by a multilevel QMC on the finest level  $L = 3$  computed with piecewise linear basis functions. The posterior expectation as clearly moved away from the prior and is located within the  $2\sigma$  region of the actual scatterer.

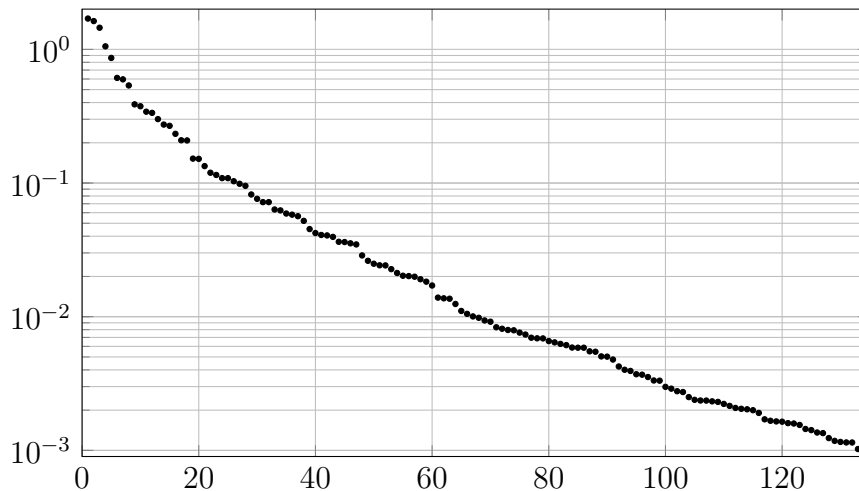


FIGURE 3. Numerical approximation of the singular values of the covariance operator under consideration.

## 8. CONCLUSIONS AND FUTURE WORK

We have introduced a fast IGA implementation for solving time-harmonic acoustic wave scattering for shape uncertainty quantification, employing boundary integral formulations, multi-level quadrature and state-of-the art acceleration techniques. This allows for the analysis of large shape deformations for both forward and inverse problems, including shape optimization. Future work involves the extension to Maxwell scattering.

## REFERENCES

- [1] R. Aylwin, C. Jerez-Hanckes, C. Schwab, and J. Zech. Domain uncertainty quantification in computational electromagnetics. *SIAM/ASA J. Uncertainty Quantification*, 8(1):301–341, 2020.
- [2] A. Barth, C. Schwab, and N. Zollinger. Multi-level Monte Carlo finite element method for elliptic PDEs with stochastic coefficients. *Numer. Math.*, 119(1):123–161, 2011.
- [3] J. Beck, L. Tamellini, and R. Tempone. IGA-based multi-index stochastic collocation for random PDEs on arbitrary domains. *Comput. Methods Appl. Mech. Eng.*, 351:330 – 350, 2019.
- [4] L. Beirão da Veiga, A. Buffa, G. Sangalli, and R. Vázquez. Mathematical analysis of variational isogeometric methods. *Acta Numer.*, 23:157–287, 2014.
- [5] A. Buffa, J. Dölz, S. Kurz, S. Schöps, R. Vázquez, and F. Wolf. Multipatch approximation of the de Rham sequence and its traces in isogeometric analysis. *Numer. Math.*, 144(1):201–236, 2020.
- [6] R. Caflisch. Monte Carlo and quasi-Monte Carlo methods. *Acta Numer.*, 7:1–49, 1998.

- [7] J. E. Castrillon-Candas, F. Nobile, and R. F. Tempone. Hybrid collocation perturbation for PDEs with random domains. *Adv. Comput. Math.*, 47:40, 2021.
- [8] D. Colton and R. Kress. *Inverse Acoustic and Electromagnetic Scattering*. Springer, Berlin-Heidelberg-New York, 2nd edition, 1997.
- [9] M. Dashti and A. M. Stuart. The bayesian approach to inverse problems. In Roger Ghanem, David Higdon, and Houman Owhadi, editors, *Handbook of Uncertainty Quantification*, pages 311–428, Cham, 2017. Springer International Publishing.
- [10] J. Dick, R. N. Gantner, Q. T. Le Gia, and C. Schwab. Multilevel higher-order quasi-Monte Carlo Bayesian estimation. *Mathematical Models and Methods in Applied Sciences*, 27(05):953–995, 2017.
- [11] J. Dölz. A Higher Order Perturbation Approach for Electromagnetic Scattering Problems on Random Domains. *SIAM/ASA Journal on Uncertainty Quantification*, 8(2):748–774, 2020.
- [12] J. Dölz, H. Harbrecht, S. Kurz, M. Multerer, S. Schöps, and F. Wolf. Bembel: Boundary element method based engineering library. <http://www.bembel.eu>.
- [13] J. Dölz, H. Harbrecht, S. Kurz, M. Multerer, S. Schöps, and F. Wolf. Bembel: The fast isogeometric boundary element C++ library for Laplace, Helmholtz, and electric wave equation. *SoftwareX*, 11:100476, 2020.
- [14] J. Dölz, H. Harbrecht, S. Kurz, S. Schöps, and F. Wolf. A fast isogeometric BEM for the three dimensional Laplace- and Helmholtz problems. *Comput. Methods Appl. Mech. Eng.*, 330(Supplement C):83–101, 2018.
- [15] J. Dölz, H. Harbrecht, and M. Peters. An interpolation-based fast multipole method for higher-order boundary elements on parametric surfaces. *Int. J. Numer. Meth. Eng.*, 108(13):1705–1728, 2016.
- [16] J. Dölz, S. Kurz, S. Schöps, and F. Wolf. Isogeometric boundary elements in electromagnetism: Rigorous analysis, fast methods, and examples. *SIAM J. Sci. Comput.*, 41(5):B983–B1010, 2019.
- [17] P. Escapil-Inchauspé and C. Jerez-Hanckes. Helmholtz scattering by random domains: First-order sparse boundary elements approximation. *SIAM J. Sci. Comput.*, 42(5):A2561–A2592, 2020.
- [18] M. Feischl, G. Gantner, A. Haberl, and D. Praetorius. Optimal convergence for adaptive IGA boundary element methods for weakly-singular integral equations. *Numer. Math.*, 136:147–182, 2017.
- [19] M. Giles. Multilevel Monte Carlo methods. *Acta Numer.*, 24:259–328, 2015.
- [20] L. Greengard and V. Rokhlin. A fast algorithm for particle simulations. *J. Comput. Phys.*, 73(2):325–348, 1987.
- [21] L. Greengard and V. Rokhlin. On the numerical solution of two-point boundary value problems. *Commun. Pure Appl. Math.*, 44(4):419–452, 1991.
- [22] W. Hackbusch and S. Börm.  $\mathcal{H}^2$ -matrix approximation of integral operators by interpolation. *Appl. Numer. Math.*, 43(1):129–143, 2002.

- [23] A.-L. Haji-Ali, H. Harbrecht, M. D. Peters, and M. Siebenmorgen. Novel results for the anisotropic sparse grid quadrature. *J. Complexity*, 47:62–85, 2018.
- [24] A.-L. Haji-Ali, H. Harbrecht, M.D. Peters, and M. Siebenmorgen. Novel results for the anisotropic sparse grid quadrature. *Journal of Complexity*, 47:62–85, August 2018.
- [25] H. Harbrecht, N. Ilić, and M. D. Multerer. Rapid computation of far-field statistics for random obstacle scattering. *Eng. Anal. Bound. Elem.*, 101:243–251, 2019.
- [26] H. Harbrecht and M. Peters. Comparison of fast boundary element methods on parametric surfaces. *Comput. Methods Appl. Mech. Eng.*, 261–262:39–55, 2013.
- [27] H. Harbrecht and M. Peters. The second order perturbation approach for elliptic partial differential equations on random domains. *Applied Numerical Mathematics*, 125:159 – 171, 2018.
- [28] H. Harbrecht, M. Peters, and R. Schneider. On the low-rank approximation by the pivoted cholesky decomposition. *Appl. Numer. Math.*, 62(4):428–440, 2012.
- [29] H. Harbrecht, M. Peters, and M. Siebenmorgen. On multilevel quadrature for elliptic stochastic partial differential equations. In J. Garcke and M. Griebel, editors, *Sparse Grids and Applications*, volume 88 of *Lecture Notes in Computational Science and Engineering*, pages 161–179, Berlin-Heidelberg, 2012. Springer.
- [30] H. Harbrecht, M. Peters, and M. Siebenmorgen. Analysis of the domain mapping method for elliptic diffusion problems on random domains. *Numer. Math.*, 134(4):823–856, 2016.
- [31] Helmut Harbrecht and Marc Schmidlin. Multilevel quadrature for elliptic problems on random domains by the coupling of FEM and BEM. *arXiv:1802.05966*, 2019. (to appear in *Stoch. Partial Differ. Equ. Anal. Comput.*).
- [32] S. Heinrich. Multilevel Monte Carlo methods. In *Lecture Notes in Large Scale Scientific Computing*, pages 58–67, London, 2001. Springer.
- [33] E. Hille and R. S. Phillips. *Functional analysis and semi-groups*. American Mathematical Society, Providence, RI, 1957.
- [34] R. Hiptmair, L. Scarabosio, C. Schillings, and Ch. Schwab. Large deformation shape uncertainty quantification in acoustic scattering. *Adv. Comput. Math.*, 44:1475–1518, 2018.
- [35] T. J. R. Hughes, J. A. Cottrell, and Y. Bazilevs. Isogeometric analysis: CAD, finite elements, NURBS, exact geometry and mesh refinement. *Comput. Methods Appl. Mech. Eng.*, 194(39):4135–4195, 2005.
- [36] C. Jerez-Hanckes and C. Schwab. Electromagnetic wave scattering by random surfaces: uncertainty quantification via sparse tensor boundary elements. *IMA Journal of Numerical Analysis*, 37(3):1175–1210, 2016.
- [37] C. Jerez-Hanckes, C. Schwab, and J. Zech. Electromagnetic wave scattering by random surfaces: Shape holomorphy. *Mathematical Models and Methods in Applied Sciences*, 27(12):2229–2259, 2017.

- [38] M. Loève. *Probability theory I+II*. Number 45 in Graduate Texts in Mathematics. Springer, New York, 4th edition, 1977.
- [39] H. Niederreiter. *Random Number Generation and Quasi-Monte Carlo Methods*. Society for Industrial and Applied Mathematics, Philadelphia, 1992.
- [40] L. Piegl and W. Tiller. *The NURBS Book*. Springer, 2nd edition, 1997.
- [41] C. Schillings and C. Schwab. Scaling limits in computational Bayesian inversion. *ESAIM: M2AN*, 50(6):1825–1856, 2016.
- [42] C. Schillings, B. Sprungk, and P. Wacker. On the convergence of the laplace approximation and noise-level-robustness of Laplace-based Monte Carlo methods for Bayesian inverse problems. *Numerische Mathematik*, 145(4):915–971, 2020.
- [43] G. Silva, R. Aylwin, C. Jerez-Hanckes, and P. Fay. Quantifying the impact of random surface perturbations on reflective gratings. *IEEE Transactions on Antennas and Propagation*, 66(2):838–847, 2018.
- [44] R. N. Simpson, S. P. A. Bordas, J. Trevelyan, and T. Rabczuk. A two-dimensional isogeometric boundary element method for elastostatic analysis. *Comput. Methods Appl. Mech. Eng.*, 209–212:87–100, 2012.
- [45] T. Takahashi and T. Matsumoto. An application of fast multipole method to isogeometric boundary element method for Laplace equation in two dimensions. *Eng. Anal. Bound. El.*, 36(12):1766–1775, 2012.
- [46] D. Tse and P. Viswanath. *Fundamentals of Wireless Communication*. Cambridge University Press, first edition, May 2005.

JÜRGEN DÖLZ, INSTITUTE FOR NUMERICAL SIMULATION, UNIVERSITY OF BONN, EN-DENICHER ALLEE 19B, 53115 BONN, GERMANY.

*Email address:* doelz@ins.uni-bonn.de

HELMUT HARBRECHT, DEPARTMENT OF MATHEMATICS AND COMPUTER SCIENCE, UNIVERSITY OF BASEL, SPIEGELGASSE 1, 4051 BASEL, SCHWEIZ.

*Email address:* helmut.harbrecht@unibas.ch

CARLOS JEREZ-HANCKES, FACULTY OF ENGINEERING AND SCIENCES, UNIVERSIDAD ADOLFO IBÁÑEZ, DIAGONAL LAS TORRES 2700, PEÑALOLÉN, SANTIAGO, CHILE.

*Email address:* carlos.jerez@uai.cl

MICHAEL MULTERER, INSTITUTE OF COMPUTATIONAL SCIENCE, USI LUGANO, VIA GIUSEPPE BUFFI 13, 6900 LUGANO, SCHWEIZ

*Email address:* michael.multerer@usi.ch



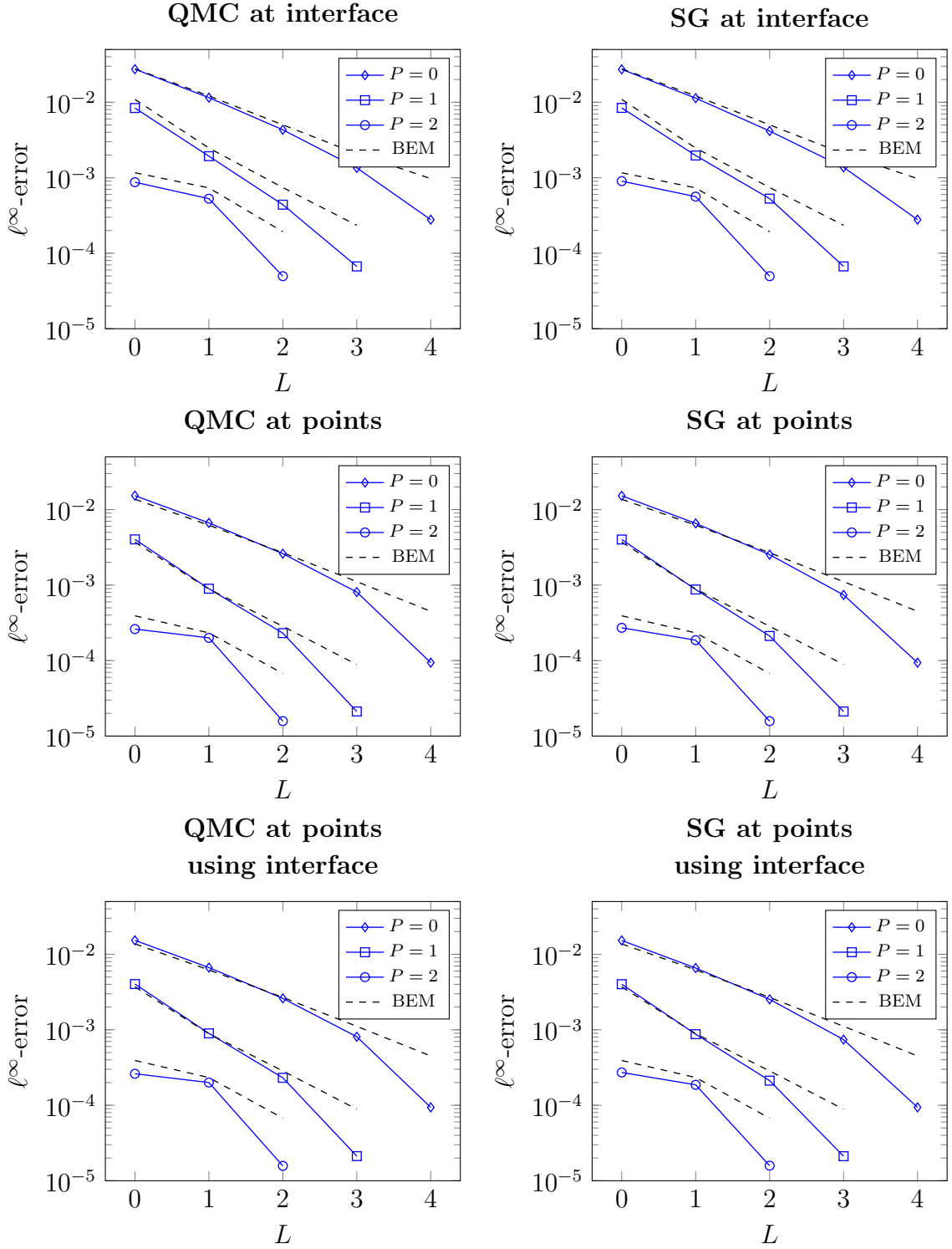


FIGURE 4. Convergence of multilevel quadratures for the expectation. *Left:* Convergence of QMC towards SG. *Right:* Convergence of SG towards QMC.

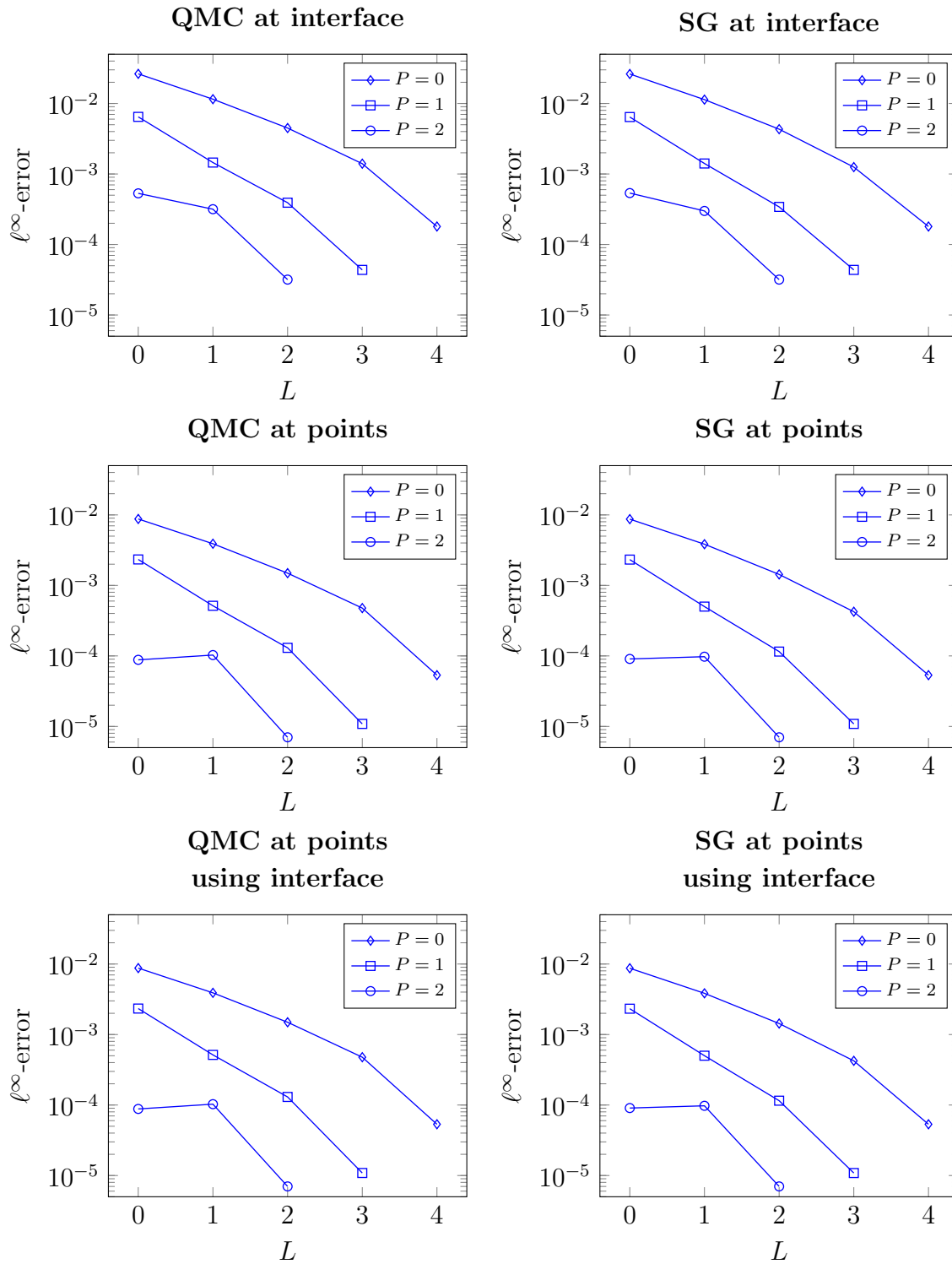


FIGURE 5. Convergence of multilevel quadratures for the correlation.  
*Left:* Convergence of QMC towards SG. *Right:* Convergence of SG towards QMC.

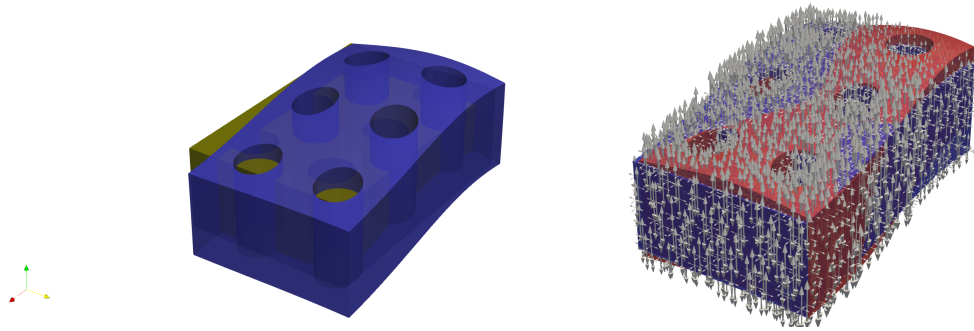


FIGURE 6. *Left:* Prior mean (yellow) and posterior mean (blue) of the inverse problem. *Right:* Reference solution (red) and posterior mean (blue) of the inverse problem with  $2\sigma$  confidence intervals (crosses) in each coordinate direction.